Featured in Physics

Sunlight-Driven Quantum Magnetometry

Yunbin Zhu,[1,3] Yijin Xie,[1,3] Ke Jing,[1,3] Ziyun Yu,[1,3] Huiyao Yu,[1,3] Wenzhe Zhang,[1,3] Xi Qin,[1,2,3] Chang-Kui Duan,[1,3] Xing Rong,[1,2,3,*] and Jiangfeng Du[1,2,3,†]

[1] *CAS Key Laboratory of Microscale Magnetic Resonance and School of Physical Sciences, University of Science and Technology of China, Hefei 230026, China*

[2] *Hefei National Laboratory, Hefei 230088, China*

[3] *CAS Center for Excellence in Quantum Information and Quantum Physics, University of Science and Technology of China, Hefei 230026, China*

(Received 21 March 2022; revised 24 July 2022; accepted 11 August 2022; published 17 October 2022)

Emerging quantum technologies, such as quantum computations and precise sensing, provide new opportunities in the fields of science and engineering. While energy consumption is a major concern for modern industry and society, it is rarely taken into consideration for quantum technologies. Especially, the potential of quantum technologies directly powered by renewable energy has long been neglected. The initialization, manipulation, and readout of quantum systems generally require high-power-consuming equipment, such as a dilution refrigerator, a microwave-power amplifier, and a high-power laser. Here, we discover a direct utilization path for solar energy to steer the quantum states of negatively charged nitrogen-vacancy centers in diamond, which is one of the most promising solid-state quantum systems in the past decades. Following this method, we demonstrate sunlight-driven quantum magnetometry. The initialization and readout of this quantum magnetometry are achieved directly by sunlight, and conventional microwave manipulation can be removed by using a microwave-free scheme. By utilizing ambient energy directly, our method brings potential solutions to the energy-consumption issue of quantum technologies. This technique can be further extended to multiple quantum systems, and thus opens the door to environmentally sustainable quantum technologies and self-powered quantum sensing in the future.

DOI: 10.1103/PRXEnergy.1.033002

I. INTRODUCTION

Quantum sensors utilize quantum systems to measure a broad range of physical quantities [1–3]. In the field of magnetometry, quantum sensors, such as a superconducting quantum interference device (SQUID) [4], an atomic magnetometer operating in a spin-exchange relaxation-free (SERF) regime [5], and a diamond magnetometer based on negatively charged nitrogen-vacancy (N-V) center ensembles [6], demonstrate outstanding sensitivity. However, the issue of their consumption of resources, especially power consumption, is rarely taken into consideration. For example, a high-power laser is usually used to initialize and read out the quantum states of quantum sensors [7–9]. Power consumption is an obstacle on the road to practical applications for quantum technologies. Besides, it is more essential than ever to save energy and find new ways to utilize renewable-energy sources while global challenges, such as climate change, increase seriously [10,11].

Here, we propose a direct utilization path for solar energy via the N-V centers in diamond and demonstrate sunlight-driven quantum magnetometry based on the magnetic-field-dependent photoluminescence (PL) of this quantum system. The N-V centers are excited by the green component of sunlight, and the conventional high-power laser is removed. The measurement is performed with a microwave-free scheme, and thus microwave manipulation is circumvented. Since the geomagnetic field is amplified by the magnetic flux concentrators (FCs) as the bias field, there is neither a permanent magnet nor an electromagnet that needs to provide an additional bias field in the setup. The quantum sensor is driven by solar energy and works without high-power-consuming equipment, such as a high-power laser and a high-power microwave amplifier. This method can bring sustainability to quantum technologies by directly utilizing ambient energy.

*xrong@ustc.edu.cn
†djf@ustc.edu.cn

II. MAGNETOMETRY METHOD

A schematic for the direct utilization path for solar energy is shown in Fig. 1. Sunlight, after being absorbed and scattered by the Earth's atmosphere, is mostly within the wavelength range of 300–1100 nm [12]. To decrease the photoinduced ionization of the N-V centers [13], filters are used to reserve sunlight with wavelengths in the range of 500–550 nm [Figs. 1(a) and 1(b)]. The light in this wavelength range can be used to steer the states of electron spins in N-V centers [14]. When the electron spins of N-V centers are excited, they will decay and emit red fluorescence [Fig. 1(c)]. The intensity of red fluorescence can be detected by a photodetector. The filters described above can also reduce the background from sunlight in the wavelength range of fluorescence. As shown in Fig. 1(d), the PL intensity is related to the external magnetic field, $\mathbf{B}_{\rm dia}$, and can be used for detecting magnetic field. In this way, we demonstrate sunlight-driven quantum magnetometry.

The quantitative magnetic field measurement based on N-V centers generally relies on the optically detected magnetic resonance (ODMR) technique [6,9]. The N-V center in diamond consists of a substitutional nitrogen atom and a vacancy on adjacent lattice sites with C_{3v} symmetry [14]. As shown in Fig. 1(c), the electronic ground state of the N-V center is a spin triplet state, $^3A_2$, with the $|m_s = 0\rangle$ state separated from the $|m_s = \pm 1\rangle$ states by a zero-field splitting of $D_{\rm GS} \approx 2.87$ GHz at room temperature. When a magnetic field, $\mathbf{B}_{\rm dia}$, is applied, the $|m_s = \pm 1\rangle$ states experience a Zeeman splitting, and the N-V ground-state electron-spin Hamiltonian can be written as [15]

$$\hat{H}_{\rm GS} = hD_{\rm GS}S_z^2 + g\mu_B\mathbf{B}_{\rm dia}\cdot\mathbf{S}, \tag{1}$$

where h is Planck's constant, μ_B is the Bohr magneton, and $g \approx 2.003$ is the electron g factor. $\mathbf{S} = (S_x, S_y, S_z)$ is the dimensionless electronic spin-1 operator, and the z direction is parallel to the N-V symmetry axis. The N-V center can be optically excited to the ^3E state, and the transition between them has a zero-phonon line at 637 nm [Γ_p in Fig. 1(c)]. Upon optical excitation, the N-V center can decay to the ground state through a spin-conserving radiative transition [Γ_0 in Fig. 1(c)], which generates red fluorescence with wavelengths in the range of 637–800 nm. There is a nonradiative alternative decay path via singlet

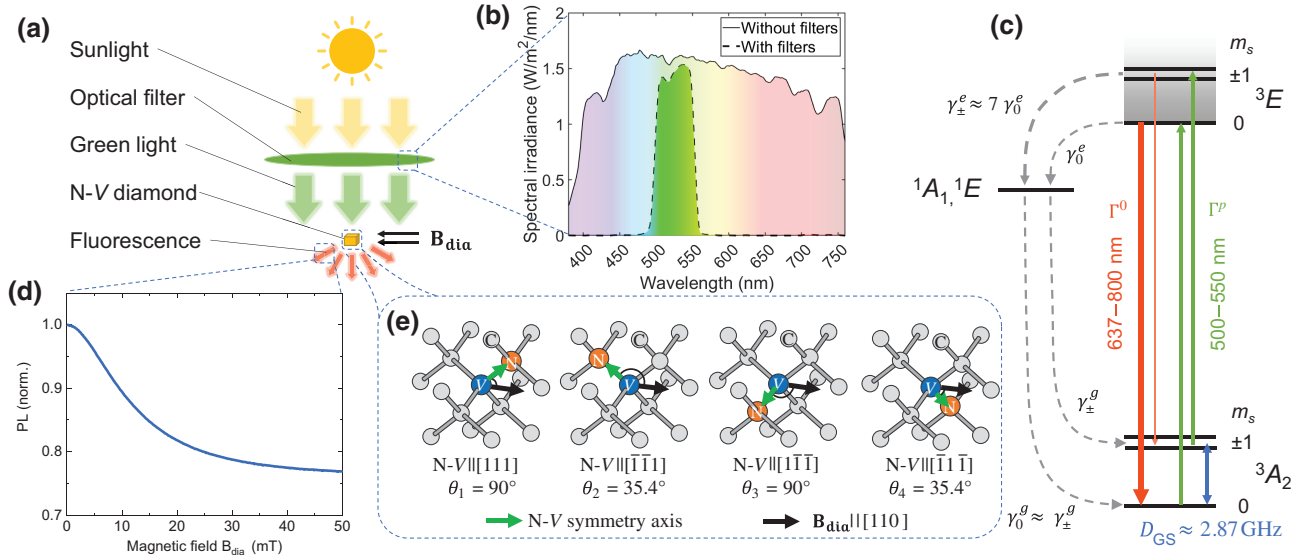

FIG. 1. Schematic of sunlight-driven magnetometry. (a) Schematic of the direct utilization path of solar energy. Sunlight is filtered and used to excite N-V centers. Intensity of fluorescence emitted from the N-V centers is related to the magnetic field, $\mathbf{B}_{\rm dia}$, on the electron spins of the N-V centers. (b) Measured spectral irradiance of sunlight with and without filters. Irradiance of sunlight with wavelengths in the range of 380–760 nm is 527 W/m^2 (solid line). After being filtered, the irradiance of residual light with wavelengths in the range of 500–550 nm is 80.6 W/m^2 (dashed line). (c) Energy-level structure of the N-V center. N-V center in the ground state can be pumped via green light to the excited state, and Γ_p is the pumping rate. Radiative relaxation results in red fluorescence, and Γ_0 is the relaxation rate. γ_0^e and $\gamma_\pm^e$ are the relaxation rates from the excited state in $|m_s = 0\rangle$ and $|m_s = \pm 1\rangle$ states to the singlet states, respectively, giving $\gamma_\pm^e \approx 7\gamma_0^e$ [19]. γ_0^g and $\gamma_\pm^g$ are the relaxation rates from the singlet states to the ground state in $|m_s = 0\rangle$ and $|m_s = \pm 1\rangle$ states, respectively, giving $\gamma_\pm^g \approx \gamma_0^g$ [19]. Under optical illumination, intensity of fluorescence resulting from the $|m_s = 0\rangle$ state (thick red arrows) is higher than that resulting from the $|m_s = \pm 1\rangle$ states (thin red arrows). (d) Simulated PL intensity as a function of $B_{\rm dia}$. PL intensity decreases with increasing $B_{\rm dia}$. (e) Four orientations of the N-V centers in diamond. When $\mathbf{B}_{\rm dia}$ along the [110] axis of diamond is applied, two of the four N-V orientations are perpendicular to $\mathbf{B}_{\rm dia}$, and the other orientations are aligned at about 35.4° with respect to $\mathbf{B}_{\rm dia}$.

states ($^1A_1$,^1E) involving nonradiative intersystem crossing (ISC) [16,17], where no red fluorescence is generated. Since the N-V center is more likely to decay through a nonradiative path when the population is in the $|m_s = \pm 1\rangle$ states [$\gamma_{\pm}^e \approx 7\gamma_0^e$ in Fig. 1(c)], the intensity of the average fluorescence from the $|m_s = 0\rangle$ state is significantly higher than that from the $|m_s = \pm 1\rangle$ states. Resonant microwave manipulation can enable the transition between the $|m_s = 0\rangle$ state and one of the less fluorescent $|m_s = \pm 1\rangle$ states and leads to the variations in fluorescence. For a certain direction of $\mathbf{B}_{\rm dia}$, the magnetic field strength, $B_{\rm dia} = |\mathbf{B}_{\rm dia}|$, can be obtained by observing the ODMR spectra.

For magnetometry, the microwave-free scheme [18–20] based on detecting changes in the magnetic-field-dependent PL of N-V centers is utilized. When a magnetic field misaligned with the N-V symmetry axis is applied, the transverse magnetic field leads to the mixing of the spin sublevels in both the ground state and excited state. The probability of a nonradiative transition involving ISC is enhanced and then results in a decrease of the PL (see the Supplemental Material [21]). For an ensemble of N-V centers, each N-V symmetry axis is oriented along one of four possible crystallographic directions [Fig. 1(e)], and the N-V symmetry axes are equally distributed along these four orientations. When $\mathbf{B}_{\rm dia}$ along the [110] crystal axis of diamond is applied, $\mathbf{B}_{\rm dia}$ is misaligned with the four orientations of N-V symmetry axes, and the PL emitted from the N-V centers decreases with increasing magnetic field strength [Fig. 1(d)]. Thus, the PL variations can be used for magnetic field measurements. Unlike the ODMR technique, this microwave-free method relies on the variation of PL with the off-axis magnetic field strength rather than the ODMR spectrum, and thus avoids the large power consumption of conventional microwave manipulation. An appropriate bias magnetic field is needed in this scheme to achieve optimal sensitivity, which is generally produced by permanent magnets [20]. Although the microwave-free scheme around the ground-state-level anticrossing (GSLAC) of the N-V center is demonstrated [22,23], it usually needs extra electromagnets or permanent magnets to produce a magnetic field of about 102.4 mT. In our work, the FCs are utilized to amplify the geomagnetic field to provide a suitable bias field with the equivalent effect of permanent magnets. More importantly, the FCs can be used to improve the sensitivity [24,25]. Our magnetometry is also compatible with both permanent magnets and FCs, and the comparison is shown in the Supplemental Material [21].

III. EXPERIMENT

The experimental setup of the sunlight-driven magnetometer is shown in Fig. 2(a). A Fresnel lens with a diameter of 15 cm is used to collect the sunlight, and a concave lens is used to adjust the focused beam. After being filtered, the light is focused by a convex lens to illuminate the diamond. With the collecting area of the Fresnel lens being about 177 cm^2, there is about 1 W light, which is used to excited the N-V centers, considering the attenuation of the focused lenses. Light is extracted

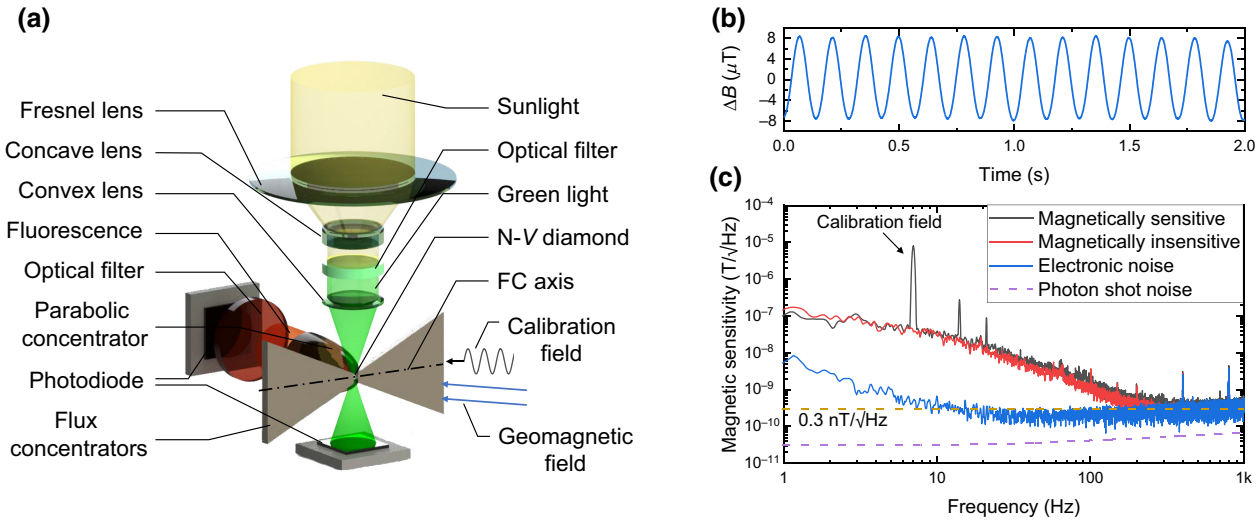

FIG. 2. Demonstration of sunlight-driven magnetometry. (a) Setup of the magnetometer. Sunlight is collected by the lenses and filtered to excite the N-V centers. Part of the light through diamond is collected by the reference PD for noise cancellation. (b) Measured time-domain magnetic signals of the magnetometer. (c) Magnetic ASDs for the time-domain signals. Magnetically sensitive spectrum (black line) shows the peak of the calibration field with a frequency of 7 Hz, and the peak is not visible in the magnetically insensitive spectrum (red line). Magnetically sensitive spectrum shows a sensitivity of 0.3 nT/$\sqrt{\rm Hz}$ @ 320 Hz. In the region above 300 Hz, electronic noise (blue line) limits the sensitivity. Photon noise (purple dashed line) of about 0.03 nT/$\sqrt{\rm Hz}$ is much less than the overall noise.

directly from sunlight, while the power consumption of a conventional laser for equivalent output light power is about 100 W, according to previous work [22]. The geomagnetic field is amplified by the FCs as the bias magnetic field for N-V centers. The (110)-cut diamond is clamped by the FCs, and the bias magnetic field direction is along the FC axis, which is aligned with the [110] crystal axis of diamond. Since the bias magnetic field direction is misaligned with the N-V axes, the level anticrossing feature is not observed or utilized. Due to the orientation response of the FCs [24], the strength of the bias magnetic field is changed by adjusting the relative direction of the FCs to the geomagnetic field orientation. The diamond is fixed to a compound parabolic concentrator, which collects the fluorescence of the N-V centers. After the fluorescence passes through a 650-nm long-pass filter, it is converted to a photocurrent via a photodetector (PD). A portion of sunlight is collected by the reference PD for noise cancellation. The PDs are set to photoconductive mode, and each one is connected to a load resistance to convert the photocurrent into a voltage signal. After that, the signals are acquired by the analog-to-digital converter (ADC).

The magnetic sensitivity of the magnetometer is measured under the geomagnetic field and an oscillating calibration field. When the bias magnetic field strength is adjusted to about 10 mT in diamond, a sinusoidal calibration field with a frequency of 7 Hz and a peak-to-peak value of 16 μT is applied via a coil. The load resistance of the PD is 10 kΩ, and the signal with a peak-to-peak value of 30 mV is recorded by the ADC [Fig. 2(b)]. The calibration factor of 1.9×10^3 V/T is then obtained. The time-domain signals under different configurations are recorded using a 2-kHz sampling rate for 30 s, and then converted into the magnetic amplitude spectral densities (ASDs). The noise for the magnetically insensitive configuration [Fig. 2(c) red line] is achieved under the bias field strength above 100 mT in diamond. The frequency response of the sensing unit is obtained from 5 to 1000 Hz, and the ASDs are calibrated accordingly (see the Supplemental Material [21]). The ASDs show the noise floor and the sensitivity of the magnetometer.

We then evaluate the noise and sensitivity of the magnetometer. For frequencies between 1 and 300 Hz, the noise exhibits nearly $1/f$ behavior. The noise might result from the power fluctuation of sunlight. Due to the frequency-response calibration, the spectrum of electronic noise [Fig. 2(c) blue line] exhibits a rising trend above 100 Hz, and electronic noise is the main noise source above 300 Hz. It can be further suppressed by using the lower noise ADC. The photon shot-noise limit [Fig. 2(c) purple dashed line] is 0.03 nT/$\sqrt{\text{Hz}}$ (see the Supplemental Material [21]) and accounts for a small part of the overall noise. With the abovementioned noise and magnetic noise, the magnetically sensitive spectrum [Fig. 2(c) black line] exhibits the best sensitivity at 320 Hz, which is 0.3 nT/$\sqrt{\text{Hz}}$. The sensitivity can be improved in future iterations by optimizing the enhancement factor of the FCs, increasing the power density of focused light and utilizing the GSLAC feature of the N-V centers for (111)-cut diamond samples. With these improvements, the sensitivity of the magnetometer can reach 0.6 pT/$\sqrt{\text{Hz}}$ (see the Supplemental Material [21]).

IV. DISCUSSION

The direction and intensity of received sunlight vary with time, and the quantitative measurements of the magnetometer need the help of a calibration field. The position of the focused light spot is related to the direction of sunlight. A solar tracking system can be used to trace the sunlight direction [26,27] and adjusts the light spot to the position of diamond. The intensity of sunlight can be measured by a reference PD. By calibrating the output signal as a function of magnetic field strength and sunlight intensity, the magnetometer can be used for quantitative measurements without a calibration field in the future.

This method of utilizing solar energy can be further extended to multiple spin-systems. According to the standard direct (AM1.5d) solar reference spectrum [28], which is defined for solar concentrator systems, the solar energy is within a broad range of wavelengths from 300 to 1100 nm. When the zero-phonon line of the transition in a spin system is within this wavelength range, sunlight can be used to steer the states of the spins. There are several spin systems that can be excited by sunlight, such as negatively charged silicon-vacancy centers (V_{Si}) in silicon carbide (SiC) [29], negatively charged germanium-vacancy centers (Ge-V) in diamond [30], and negatively charged silicon-vacancy centers (Si-V) in diamond [31](see Supplemental Material [21]). Furthermore, other undiscovered potential quantum systems with similar energy-level structures can also be combined with this scheme.

In conclusion, we reveal a direct utilization path of solar energy to steer the quantum states of N-V centers in diamond and demonstrate sunlight-driven quantum magnetometry. The green light for exciting the N-V centers is extracted from sunlight directly. Power consumption of about 100 W for the high-power laser can be avoided. The demonstrated quantum magnetometer can be extended as autonomous and self-powered magnetic field sensor nodes used in geomagnetic observation and Internet of things applications for extremely-low-frequency (ELF, 0.1–300 Hz) signal detection [32–34]. In outer space, the intensity of sunlight is stronger than that on the ground, as a result of the lack of absorption and scattering by the atmosphere. Such a magnetometer with optimization in the detection range (see the Supplemental Material [21]) has potential for space-based applications [35,36]. For this purpose, the remaining components of sunlight, except those that are directly utilized for quantum systems, can be collected

to power traditional electronic devices for signal processing by solar-energy harvesters in the future [37,38]. It is worth mentioning that using a laser diode powered by solar panels can also yield green light to excite the N-V centers. However, the efficiency of our method is 3 times as much as that of this method (see the Supplemental Material [21]), since energy loss due to energy conversion can be avoided. The efficiency is defined as the ratio of utilized green-light power to total input solar power. This direct utilization path of renewable energy thus exhibits higher efficiency than traditional laser excitation to achieve initialization and readout for the quantum sensor. Albeit a small step for today's quantum sensors, directly utilizing ambient energy is a possible approach to solve the power-consumption issue of quantum technologies. Additionally, this method exhibits the potential of quantum technologies in renewable-energy utilization and could make a contribution to sustainable development [39–41].

ACKNOWLEDGMENTS

This work is supported by the Chinese Academy of Sciences (Grants No. XDC07000000, No. GJJSTD20200001, No. QYZDY-SSW-SLH004, and No. QYZDB-SSW-SLH005), the National Key R&D Program of China (Grants No. 2018YFA0306600 and No. 2016YFB050 1603), the National Natural Science Foundation of China (Grant No. 81788101), the Innovation Program for Quantum Science and Technology (Grants No. 2021ZD0302200 and No. 2021ZD0303204), the Anhui Initiative in Quantum Information Technologies (Grant No. AHY050000), and the Hefei Comprehensive National Science Center. X.R. thanks the Youth Innovation Promotion Association of Chinese Academy of Sciences for support.

Y.Z., Y.X., and K.J. contributed equally to this work. J.D. and X.R. proposed the idea and supervised the experiments. Y.Z., Y.X., and K.J. designed and performed the experiments. H.Y. prepared the sample. W.Z. and X.Q. developed the home-built lock-in amplifier. Y.Z., Y.X., C.D., and K.J. carried out the simulations. All authors contributed to the preparation of the manuscript. All authors analyzed data, discussed the results, and commented on the manuscript.

[1] C. L. Degen, F. Reinhard, and P. Cappellaro, Quantum sensing, Rev. Mod. Phys. **89**, 035002 (2017).

[2] S. Pirandola, B. R. Bardhan, T. Gehring, C. Weedbrook, and S. Lloyd, Advances in photonic quantum sensing, Nat. Photonics **12**, 724 (2018).

[3] M. W. Mitchell and S. P. Alvarez, Colloquium: Quantum limits to the energy resolution of magnetic field sensors, Rev. Mod. Phys. **92**, 021001 (2020).

[4] M. Schmelz, R. Stolz, V. Zakosarenko, T. Schönau, S. Anders, L. Fritzsch, M. Mück, and H. Meyer, Field-stable SQUID magnetometer with sub-fT $Hz^{-1/2}$ resolution based on sub-micrometer cross-type Josephson tunnel junctions, Supercond. Sci. Technol. **24**, 065009 (2011).

[5] H. Dang, A. C. Maloof, and M. V. Romalis, Ultrahigh sensitivity magnetic field and magnetization measurements with an atomic magnetometer, Appl. Phys. Lett. **97**, 151110 (2010).

[6] T. Wolf, P. Neumann, K. Nakamura, H. Sumiya, T. Ohshima, J. Isoya, and J. Wrachtrup, Subpicotesla Diamond Magnetometry, Phys. Rev. X **5**, 041001 (2015).

[7] J. M. Schloss, J. F. Barry, M. J. Turner, and R. L. Walsworth, Simultaneous Broadband Vector Magnetometry Using Solid-State Spins, Phys. Rev. Appl. **10**, 034044 (2018).

[8] T. Ruster, H. Kaufmann, M. A. Luda, V. Kaushal, C. T. Schmiegelow, F. Schmidt-Kaler, and U. Poschinger, Entanglement-Based dc Magnetometry with Separated Ions, Phys. Rev. X **7**, 031050 (2017).

[9] J. F. Barry, M. J. Turner, J. M. Schloss, D. R. Glenn, Y. Song, M. D. Lukin, H. Park, and R. L. Walsworth, Optical magnetic detection of single-neuron action potentials using quantum defects in diamond, Proc. Natl. Acad. Sci. **113**, 14133 (2016).

[10] O. Hoegh-Guldberg, D. Jacob, M. Taylor, T. G. Bolaños, M. Bindi, S. Brown, I. A. Camilloni, A. Diedhiou, R. Djalante, K. L. Ebi *et al.*, The human imperative of stabilizing global climate change at 1.5°C, Science **365**, 6459 (2019).

[11] F. F. Nerini, B. Sovacool, N. Hughes, L. Cozzi, E. Cosgrave, M. Howells, M. Tavoni, J. Tomei, H. Zerriffi, and B. Milligan, Connecting climate action with other sustainable development goals, Nat. Sustainability **2**, 674 (2019).

[12] Y. A. Eltbaakh, M. Ruslan, M. Alghoul, M. Othman, K. Sopian, and M. Fadhel, Measurement of total and spectral solar irradiance: Overview of existing research, Renewable Sustainable Energy Rev. **15**, 1403 (2011).

[13] N. Aslam, G. Waldherr, P. Neumann, F. Jelezko, and J. Wrachtrup, Photo-induced ionization dynamics of the nitrogen vacancy defect in diamond investigated by single-shot charge state detection, New J. Phys. **15**, 013064 (2013).

[14] M. W. Doherty, N. B. Manson, P. Delaney, F. Jelezko, J. Wrachtrup, and L. C. Hollenberg, The nitrogen-vacancy colour centre in diamond, Phys. Rep. **528**, 1 (2013).

[15] J. F. Barry, J. M. Schloss, E. Bauch, M. J. Turner, C. A. Hart, L. M. Pham, and R. L. Walsworth, Sensitivity optimization for NV-diamond magnetometry, Rev. Mod. Phys. **92**, 015004 (2020).

[16] M. L. Goldman, A. Sipahigil, M. Doherty, N. Y. Yao, S. Bennett, M. Markham, D. Twitchen, N. Manson, A. Kubanek, and M. D. Lukin, Phonon-Induced Population Dynamics and Intersystem Crossing in Nitrogen-Vacancy Centers, Phys. Rev. Lett. **114**, 145502 (2015).

[17] M. L. Goldman, M. Doherty, A. Sipahigil, N. Y. Yao, S. Bennett, N. Manson, A. Kubanek, and M. D. Lukin, State-selective intersystem crossing in nitrogen-vacancy centers, Phys. Rev. B **91**, 165201 (2015).

[18] R. Epstein, F. Mendoza, Y. Kato, and D. Awschalom, Anisotropic interactions of a single spin and dark-spin spectroscopy in diamond, Nat. Phys. **1**, 94 (2005).

[19] J. Tetienne, L. Rondin, P. Spinicelli, M. Chipaux, T. Debuisschert, J. Roch, and V. Jacques, Magnetic-field-dependent photodynamics of single NV defects in diamond:

An application to qualitative all-optical magnetic imaging, New J. Phys. **14**, 103033 (2012).

[20] D. Paone, D. Pinto, G. Kim, L. Feng, M.-J. Kim, R. Stöhr, A. Singha, S. Kaiser, G. Logvenov, B. Keimer, J. Wrachtrup, and K. Kern, All-optical and microwave-free detection of Meissner screening using nitrogen-vacancy centers in diamond, J. Appl. Phys. **129**, 024306 (2021).

[21] See the Supplemental Material at http://link.aps.org/supplemental/10.1103/PRXEnergy.1.033002 for additional experimental and magnetometry details, which include Refs. [19,24,25,42]; future improvement in sensitivity, which includes Refs. [22,25,43]; optimization in future applications, which include Refs. [44,45]; and extension to multiple spin-systems, which include Refs. [28–31]; and efficiency and power-consumption comparisons, which include Refs. [28,46–52].

[22] H. Zheng, Z. Sun, G. Chatzidrosos, C. Zhang, K. Nakamura, H. Sumiya, T. Ohshima, J. Isoya, J. Wrachtrup, A. Wickenbrock, and D. Budker, Microwave-Free Vector Magnetometry with Nitrogen-Vacancy Centers along a Single Axis in Diamond, Phys. Rev. Appl. **13**, 044023 (2020).

[23] G. Chatzidrosos, J. S. Rebeirro, H. Zheng, M. Omar, A. Brenneis, F. M. Stürner, T. Fuchs, T. Buck, R. Rölver, T. Schneemann, P. Blümler, D. Budker, and A. Wickenbrock, Fiberized diamond-based vector magnetometers, Front. Photonics **2**, 732748 (2021).

[24] I. Fescenko, A. Jarmola, I. Savukov, P. Kehayias, J. Smits, J. Damron, N. Ristoff, N. Mosavian, and V. M. Acosta, Diamond magnetometer enhanced by ferrite flux concentrators, Phys. Rev. Res. **2**, 023394 (2020).

[25] Y. Xie, H. Yu, Y. Zhu, X. Qin, X. Rong, C.-K. Duan, and J. Du, A hybrid magnetometer towards femtotesla sensitivity under ambient conditions, Sci. Bull. **66**, 127 (2021).

[26] W. Nsengiyumva, S. G. Chen, L. Hu, and X. Chen, Recent advancements and challenges in solar tracking systems (STS): A review, Renewable Sustainable Energy Rev. **81**, 250 (2018).

[27] M. E. Chowdhury, A. Khandakar, B. Hossain, and R. Abouhasera, A low-cost closed-loop solar tracking system based on the sun position algorithm, J. Sens. **2019**, 3681031 (2019).

[28] The American Society for Testing and Materials. Standard tables for reference solar spectral irradiances. *Standard G173-03* (2003).

[29] R. Nagy, M. Niethammer, M. Widmann, Y. Chen, P. Udvarhelyi, C. Bonato, J. U. Hassan, R. Karhu, I. G. Ivanov, N. T. Son *et al.*, High-fidelity spin and optical control of single silicon-vacancy centres in silicon carbide, Nat. Commun. **10**, 1954 (2019).

[30] M. K. Bhaskar, D. D. Sukachev, A. Sipahigil, R. E. Evans, M. J. Burek, C. T. Nguyen, L. J. Rogers, P. Siyushev, M. H. Metsch, H. Park, F. Jelezko, M. Lončar, and M. D. Lukin, Quantum Nonlinear Optics with a Germanium-Vacancy Color Center in a Nanoscale Diamond Waveguide, Phys. Rev. Lett. **118**, 223603 (2017).

[31] T. Müller, C. Hepp, B. Pingault, E. Neu, S. Gsell, M. Schreck, H. Sternschulte, D. Steinmüller-Nethl, C. Becher, and M. Atatüre, Optical signatures of silicon-vacancy spins in diamond, Nat. Commun. **5**, 3328 (2014).

[32] O. Avatefipour and F. Sadry, in *2018 IEEE International Conference on Electro/Information Technology (EIT)*, (IEEE, Rochester, MI, USA, 2018), p. 1041.

[33] P. Kotzé, P. Cilliers, and P. Sutcliffe, The role of SANSA's geomagnetic observation network in space weather monitoring: A review, Space Weather **13**, 656 (2015).

[34] F.-H. Zheng and Q.-Y. Di, Propagation of ELF electromagnetic waves over a curved stratified ground and its application in geophysical prospecting, IEEE Access **9**, 145563 (2021).

[35] N. Olsen, E. Friis-Christensen, R. Floberghagen, P. Alken, C. D. Beggan, A. Chulliat, E. Doornbos, J. T. Encarnação, B. Hamilton, G. Hulot *et al.*, The Swarm satellite constellation application and research facility (SCARF) and Swarm data products, Earth, Planets Space **65**, 1189 (2013).

[36] Y. Zou, Y. Zhu, Y. Bai, L. Wang, Y. Jia, W. Shen, Y. Fan, Y. Liu, C. Wang, A. Zhang *et al.*, Scientific objectives and payloads of Tianwen-1, China's first Mars exploration mission, Adv. Space Res. **67**, 812 (2021).

[37] H. Sharma, A. Haque, and Z. A. Jaffery, Solar energy harvesting wireless sensor network nodes: A survey, J. Renewable Sustainable Energy **10**, 023704 (2018).

[38] Y. Li and R. Shi, An intelligent solar energy-harvesting system for wireless sensor networks, EURASIP J. Wireless Commun. Networking **2015**, 1 (2015).

[39] D. Griggs, M. Stafford-Smith, O. Gaffney, J. Rockström, M. C. Öhman, P. Shyamsundar, W. Steffen, G. Glaser, N. Kanie, and I. Noble, Sustainable development goals for people and planet, Nature **495**, 305 (2013).

[40] S. Mallapaty, How china could be carbon neutral by mid-century, Nature **586**, 482 (2020).

[41] Z. Xu, S. N. Chau, X. Chen, J. Zhang, Y. Li, T. Dietz, J. Wang, J. A. Winkler, F. Fan, B. Huang *et al.*, Assessing progress towards sustainable development over space and time, Nature **577**, 74 (2020).

[42] D. C. Jiles, Modelling the effects of eddy current losses on frequency dependent hysteresis in electrically conducting media, IEEE Trans. Magn. **30**, 4326 (1994).

[43] S. V. Anishchik and K. L. Ivanov, A method for simulating level anti-crossing spectra of diamond crystals containing N*V*-color centers, J. Magn. Reson. **305**, 67 (2019).

[44] C. Reigber, H. Lühr, and P. Schwintzer, Announcement of opportunity for CHAMP (2001).

[45] B. Cheng, B. Zhou, W. Magnes, R. Lammegger, and A. Pollinger, High precision magnetometer for geomagnetic exploration onboard of the China seismo-electromagnetic satellite, Sci. China Technol. Sci. **61**, 659 (2018).

[46] SunPower Corporation. Maxeon 3 datasheet. *MAXEON 3 Datasheet* (2019).

[47] Nichia Corporation. NDG7D75 datasheet. *NDG7D75 Datasheet*.

[48] A. Grosz, M. J. Haji-Sheikh, and S. C. Mukhopadhyay, *High Sensitivity Magnetometers* (Springer International Publishing, Cham, Switzerland, 2017).

[49] A. Herrera-May, P. J. García-Ramírez, L. A. Aguilera-Cortés, J Martínez-Castillo, A Sauceda-Carvajal, L García-González, and E Figueras-Costa, A resonant magnetic field

microsensor with high quality factor at atmospheric pressure, J. Micromech. Microeng. **19**, 015016 (2008).

[50] A. Herrera-May, P. J. García-Ramírez, L. A. Aguilera-Cortés, E. Figueras, J. Martinez-Castillo, E. Manjarrez, A. Sauceda, L. García-González, and R. Juárez-Aguirre, Mechanical design and characterization of a resonant magnetic field microsensor with linear response and high resolution, Sens. Actuators A: Phys. **165**, 399 (2011).

[51] P. Minotti, S. Brenna, G. Laghi, A. G. Bonfanti, G. Langfelder, and A. L. Lacaita, A sub-400-nT/$\sqrt{\text{Hz}}$, 775-μW, multi-loop MEMS magnetometer with integrated readout electronics, J. Microelectromech. Syst. **24**, 1938 (2015).

[52] D. Krawat, M. Marx, S. Nessler, H. Biegler, M. Dienger, J. Rockstroh, A. Dehe, and Y. Manoli, in *2019 IEEE SENSORS* (IEEE, Montreal, QC, Canada, 2019), p. 1.